The effect of Rotor Separation on the Performance of a Dual Rotor Wind Turbine

*Dr. Adeyanju Anthony Ademola, Omar Mohammed, Dr. Manohar Krishpersad

Mechanical and Manufacturing Engineering Department, University of West Indies,
St. Augustine, Trinidad and Tobago.
Email: anthony.adeyanju@sta.uwi.edu

Abstract

This study conducted simulation and experimental analysis on a dual rotor horizontal axis wind turbine to determine the effect of rotor separation on its performance.

An air study was conducted to optimize the turbine blades to a local climate of Trinidad, it was determined that a NACA 64-315 air foil would be the most optimum for the conditions.

QBlade software was used for the simulation, the power flow performance for multiple iterations of wind speed was found for the design.

The effect of rotor separation on the performance of the dual rotor wind turbine was studied with rotor separation 0.25 m to 3.0 m at an interval of 0.25 m and it was discovered that the smallest rotor separation 0.25 m shows the largest tip speed ratio, while the largest rotor separation distance 3m has the smallest tip speed ratio at a fan speed of 1m/s. Also, as the rotor separation decreases the power coefficient (C_P) and the total power increase, which resulted to high energy output of the DRHAWT. This result is valid for the QBlade simulations and the experimental results.

Keywords: *Dual rotor, Rotor separation, Power Coefficient, QBlade software.*

1. Introduction

Global fossil-fuel reserves have been rapidly depleted in recent decades, increasing environmental concerns. As a result, for global energy stability, the emphasis has shifted to environmentally sustainable and renewable sources. Renewable energy sources, such as hydro, solar, wind, bioenergy, geothermal, and others, were built and optimized to achieve

long-term power generation. According to the International Renewable Energy Agency (IRENA), a global renewable energy (GRE) capacity reached 2537 GW at the end of 2019, accounting for 34.7 percent of net global energy (NGE) capacity [1], reflecting a 7.4 percent (176 GW) rise from 2018, when wind energy contributed 2.5 percent [1]. As a result, the Global Wind Energy Council (GWEC) announced a 10% rise in global wind energy (GWE) capacity at the end of 2019, with an average growth rate of 9.2 percent projected over the next five years [2]. The demand for larger turbines has been seen to lead to such a forecast in wind energy development. Modern multi-megawatt wind turbines have a diametric scale of more than 200 m and can produce up to 15 MW of power [3].

Wind turbines actually harness the kinetic energy of the wind with a single rotor. Though dual rotor wind turbines are well-known, these wind turbines use counter-rotating propellers to generate a single power output. Furthermore, the propellers are of a single dimension, which does not allow for the most effective usage of all usable wind energy. Since the rotor derives power from the kinetic energy of the wind, the airstream after the first rotor on a wind turbine travel slower than the airstream before the first rotor which indicates that the airstream after the rotor is larger. The second rotor should be larger to capture this wind as well as the extra wind moving through the first rotor. Furthermore, there is an unmet demand for producing multiple types of power from a single wind turbine, such as different voltages or combinations of AC and DC electrical power, or operating multiple combinations of generators, pumps, and compressors.

As a result, a dual rotor wind turbine that effectively harnesses the kinetic energy of the wind, and that can withstand various wind speeds is desirable.

Many research papers on dual rotor wind energy usage have been published, but most of the researchers have used the counter rotating rotor in their research. Kumar et al. found that using a counter rotor with a different diameter and positioning a primary rotor at a different position (0.3 d to 0.65 d) increased power output by up to 9.67% [4]. Jung et al. [5] calculated

the power curve for a 30 KW CRTWT device, as well as the effect of distance and diameter between the dual rotors.

On a counter rotating wind turbine, Oprina et al. [6] measured and analyzed the Rotor performance. The power coefficient of multiple or dual rotors of the same radius can be increased by approximately 13% compared to a single rotor, according to theoretical calculations. Flow visualization revealed misleading findings from a distance equal to half of a disc diameter, indicating the paper's limitations. A theoretical model is proposed that considers two co-axial rotors smaller than the front rotor and positioned around the inner blade region of the front rotor to increase power extraction from wind [7, 8]. Since there are no blades in the central part of the upstream rotor (76.2 percent of the rotor diameter), it does not extract wind energy. The theoretical power coefficient depends on the induction velocities, according to further calculations. The overall power coefficient for the investigated case was 0.814. Compared to a single rotor situation, the device is more effective at low rotational speeds (16−60 rpm), the energy extracted from the wind will increase by up to 40%, and the bending stress over the tower is reduced [9]. According to simulations, the secondary rotor turbine should be 25% the size of the main rotor, and it should be axially isolated from the main rotor by 0.2 times the main rotor radius to achieve a net of 7% in power coefficient [10].

Milind Deotale [11] found that the overall system's efficiency peaks at 60 percent at higher wind speeds, but then drops to 28 percent from 30 percent at lower wind speeds. However, at top speeds, average performance is 45 percent.

This study conducted simulation and experimental analysis on a designed dual rotor horizontal axis wind turbine (DRHAWT) to determine the effect of rotor separation on its performance.

2. Performance Models Estimation

To estimate the performance model, two performance models were used, the 2-dimensional Blade Element Momentum Theory which can be done by hand calculations and 3d

dimensional Prandtl Post-Stall, which accounts for rotational losses. The Post-Stall model will be done for simulation in Q blade, as it requires a large number of iterations and data input. These methods are typically used for single rotor turbines to analyze the local rotation; however, the wake velocity induced can be used as the entering velocity for the second rotor modified using the Jensen Wake Model [12]. To determine the ideal tip speed ratio, an assumption was made for the chord (c) then the blade chord length can be adjusted to determine the tip speed ratio. The specifications used for the dual rotor wind turbine is as shown in Table 1.

Table 1. Specifications of the dual rotor wind turbine [12]

Rotor Parameters	Primary Rotor	Secondary Rotor
Number of Blades (N_b)	3	3
Blade Length (m)	0.5	0.5
Rotor Position	Upwind	Downwind
Airfoil	NACA 64-315	NACA 64-315
Angle of Attack (α) (°)	6	-6
Rotation	Clockwise	Counter-Clockwise
Twist (β) (°)	5	5

2.1. Blade Element Momentum (BEM) Theory

The BEM model using the core physics of the momentum theory with the more realistic assumption of dividing the blade into an infinitesimal number of sections (*dr*). Thus, based on the concept of angular momentum conservation, the change in axial force can be defined as:

$$dN = \frac{\frac{\rho}{2} * V_0^{\,2}(1-a)^2}{\sin^2 \varnothing} N_b \left(C_L \cos \varnothing + C_D \sin \varnothing\right) c dr \quad \text{.....(1)}$$

Where, ϕ (α+β) is the flow angle, V_0 is the far upstream wind velocity and c is the airfoil chord. The torque generated by an element of *dr* can be defined as:

$$dT = \frac{\frac{\rho}{2} * V_0(1-a)}{\sin\varnothing} \frac{\omega r(1+a')}{\cos\varnothing} N_b (C_L \cos\varnothing - C_D \sin\varnothing) crdr \quad \text{.....(2)}$$

Where, ω is the rotational velocity of the element, and r is the local rotor radius.

From airfoil selection, at an angle of attack of 6º the C_L and the C_D of an NACA 64–315 is 0.7735 and 0.006344 respectively.

Another important parameter that was determined in the performance model is the axial and tangential factors (a and a') written as:

$$a = \frac{1}{\frac{4F\sin^2\varnothing}{\frac{cN_b}{2\pi r}(C_L\cos\varnothing + C_D\sin\varnothing)} + 1} \quad \text{.....(3)}$$

$$a' = \frac{1}{2}\left[\left(\sqrt{1+\frac{4}{\lambda_r^2}a(1-a)}\right)-1\right] \quad \text{.....(4)}$$

Where, λ_r is the local tip speed ratio, F is the Prandtl's Tip Loss Factor given by:

$$F = \frac{2}{\pi}\cos^{-1}\left(e^{\frac{-N_b(R-r)}{2r\sin\phi}}\right) \quad \text{.....(5)}$$

Using these equations, the values for F, a and a' for different values of λ (tip speed ratio) was determined. Once *'a'* has been obtained from each section, the overall rotor power coefficient determined using equation (6) [13]:

$$C_p = \left(\frac{8}{\lambda^2}\right)\int_{\lambda_r}^{\lambda} \lambda_r a'(1-a)\left[1-\left(\frac{C_d}{C_l}\right)\cot\phi\right] d\lambda_r \quad \text{.....(6)}$$

By varying the tip speed ratio, the estimated power coefficients are shown in Table 2.

Table 2. Estimated Power Coefficients for the Primary Rotor

Tip Speed Ratio, *λ*	3	5	7	9	11	13
Power Coefficient *Cp*	0.4291	0.5023	0.5387	0.5645	0.5744	0.5813
$\frac{\delta C_p}{\delta\lambda}$	-	0.0366	0.0182	0.0129	0.0050	0.00343

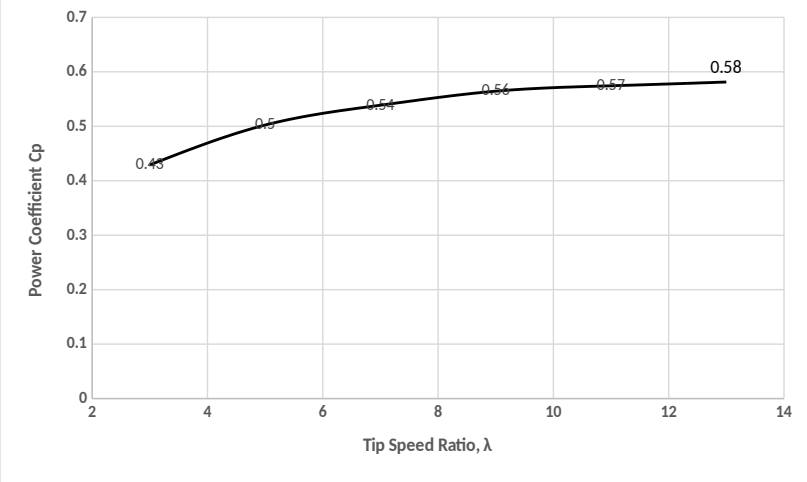

Figure 1. Estimated Power Coefficients for the Primary Rotor

Figure 1 shows that as tip speed ratio increases, the power coefficient increases as well. It can be concluded that as $\lambda \rightarrow \infty$ C_p converges to Betz Limit (0.593). However, high tip speed ratios result in large cyclic loads and unstable rotational forces that could cause mechanical failures in high-speed winds, as a result a tip speed ratio of 9 as it strikes a balance between highest C_p and greatest differential value.

From the value of λ, the axial induction factor 'a', and thrust coefficient, C_t was determined as:

$C_t = 0.6086$; $a = 0.1904$

Using the value of '*a*' the relationship between the velocities entering and exiting the rotor was determined as:

$v_2 = v_1(1\text{-}2a) \rightarrow v_2 = 0.6192v_1$

However, the velocity entering the secondary rotor would not be the same as a free velocity of the same magnitude as the wake induced velocity would experience vortices and eddy currents induced by turbulence from the high-pressure regions of the rotor's tips. Therefore, the Jensen Wake Model [12] was used to determine the difference by the actuator disk prediction and the wake-induced value:

$$\delta v_w = v_2\left(1-\sqrt{1-C_t}\right)\left(\frac{D}{D+2k_w x}\right)\frac{A_{overlap}}{A} \quad \text{.....(7)}$$

Where, 'D' is the rotor diameter, 'x' is the horizontal distance between the disks, 'k_w' is the wake decay constant and $A_{overlap}$ is the area of the second disk covered by the first disk's area 'A'. As the two rotors are coaxial, the ratio between the areas is one.

The wake decay constant is:

$$k_w = \frac{0.5}{\ln\left(\frac{h}{z_0}\right)} \quad \text{.....(8)}$$

$$z_0 = e^{\frac{u_{2\ln}(h_2)-u_1\ln(h_1)}{u_2-u_1}} \quad \text{.....(9)}$$

Where, h is the hub height of the turbine and z_0 is the roughness parameter (u is the air velocity at a given height, h).

From equation (8) and (9) the difference in wake velocity as a function of v_1 was calculated by computing z_0 using wind values from the wind study conducted in the study (v = 3.79 m/s h = 20 m) and metrological data obtained from the Trinidad and Tobago Metrological Service [14] (v= 3.2 m/s h = 10 m).

This gives a value of: $Z_0 = 859.11$; $k_w = -0.133$; $\delta v_w = \frac{0.3744\, v_2}{1-0.266\, x}$

Thus, the velocity incoming into the second rotor as a function of the incoming wind speed and the rotor separation distance was determined as:

$$v_{sec_{rotor}} = 0.6192\, v_1\left(1-\frac{0.3744}{1-0.266\, x}\right) \quad \text{.....(10)}$$

To determine the C_p for the second rotor by using the same method as above but, for a flow angle of -1° and new lift drag coefficients of 0.8498 and 0.002245 respectively, the power coefficient for the second turbine was determined as shown in Table 3.

Table 3: Estimated Power Coefficients of the Secondary Rotor

Tip Speed Ratio, λ	3	5	7	9	11	13

Power Coefficient Cp	0.2876	0.3124	0.3453	0.3893	0.4094	0.4165
$\frac{\delta C_p}{\delta \lambda}$	-	0.0124	0.0165	0.022	0.01005	0.00705

From Table 3, a tip speed ratio of 9 for the secondary rotor was chosen.

Therefore, Power gained by the entire turbine as a function of incoming wind velocity, v_1:

$$P = P_{pri_{rotor}} + P_{sec_{rotor}} \quad \text{.....(11)}$$

$$P = Cp_{pri}\frac{1}{2}\rho A\, v_1^{\,3} + Cp_{sec}\frac{1}{2}\rho A * \left(0.6192\, v_1\left(1 - \frac{0.3744}{1 - 0.266\, x}\right)\right)^3 \quad \text{.....(12)}$$

The output power was expressed using different values for v_1 and x. Table 4 shows the potential power output varying with wind velocity and rotor separation.

Table 4: Potential Power Output varying with wind velocity and rotor separation

		Output Power of System (W)									
	Rotor Separation (m)	**0.25**	**0.5**	**0.75**	**1**	**1.25**	**1.5**	**1.75**	**2**	**2.25**	**2.5**
Wind Velocity (m/s)											
1		0.36	0.36	0.36	0.35	0.35	0.35	0.35	0.35	0.35	0.35
2		2.88	2.86	2.85	2.83	2.82	2.80	2.79	2.78	2.78	2.78
3		9.70	9.65	9.61	9.55	9.50	9.46	9.41	9.39	9.37	9.37
4		23.00	22.89	22.77	22.65	22.53	22.41	22.32	22.25	22.22	22.21
5		44.92	44.70	44.47	44.23	44.00	43.78	43.59	43.45	43.40	43.38
6		77.63	77.24	76.84	76.43	76.03	75.65	75.32	75.09	74.99	74.96
7		123.27	122.65	122.02	121.37	120.73	120.12	119.60	119.23	119.08	119.04
8		184.00	183.08	182.14	181.17	180.21	179.31	178.53	177.98	177.76	177.69
9		261.99	260.68	259.34	257.95	256.59	255.31	254.20	253.42	253.10	253.00
10		359.38	357.58	355.74	353.85	351.98	350.22	348.69	347.62	347.18	347.05

11		478.33	475.94	473.49	470.97	468.49	466.14	464.11	462.69	462.10	461.93
12		621.01	617.90	614.72	611.45	608.22	605.17	602.54	600.69	599.94	599.71
13		789.55	785.61	781.56	777.40	773.30	769.42	766.08	763.73	762.77	762.48
14		986.13	981.21	976.15	970.96	965.83	960.99	956.82	953.88	952.68	952.32
15		1212.90	1206.84	1200.63	1194.23	1187.93	1181.98	1176.85	1173.23	1171.75	1171.31
16		1472.01	1464.66	1457.12	1449.36	1441.71	1434.48	1428.25	1423.86	1422.07	1421.53

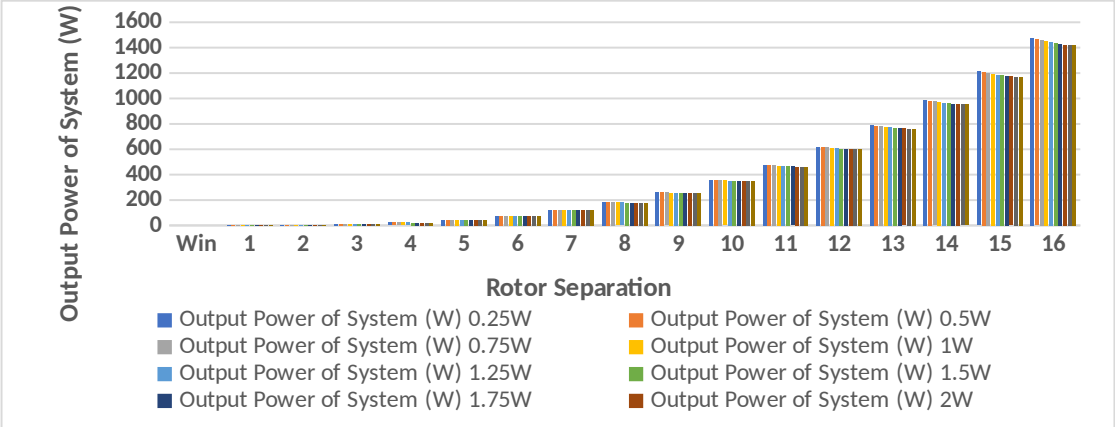

Figure 2: Potential Power Output varying with wind velocity and rotor separation

The maximum output power occurs at the fastest wind speed and the smallest rotor separation distance as shown in Figure 2. Therefore, the rotors should be close as physically possible to each other to allow for maximum power gain.

By comparing this value to the maximum power that was extracted from the wind, the C_p for the entire system assuming a rotor distance of 0.25 m was determined as:

$$C_p = \frac{Cp_{pri}\frac{1}{2}\rho A(v_1)^3 + Cp_{sec}\frac{1}{2}\rho A * \left(0.6192\, v_1\left(1-\frac{0.3744}{1-0.266\,x}\right)\right)^3}{\frac{1}{2}\rho A\, v_1^{\,3}} \quad \text{.....(13)}$$

$\therefore C_p = 58.69\%$.

According to the blade element theory, 58.69% of the wind's kinetic energy can be extracted.

2.2. Stall Model Simulation

Using Qblade, the two rotors were modeled, this time accounting for 3d correction loss as well as root loss and tip loss.

2.2.1. Primary Rotor

Using the previous boundary conditions, the ideal tip speed ratio for our blade was determined. A maximum of 1000 iterations, Rho = 1.23 and a relaxation factor of 0.3, the simulation was plotted for angles of attack ranging from −10º to 15º with a delta of 0.5 degrees (Figure 3).

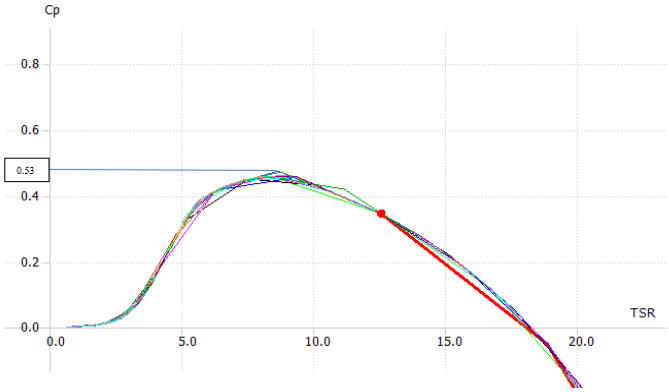

Figure 3. Relationship between the power coefficient and Tip speed ratio for the Primary Rotor

From the simulation, a maximum power coefficient (Cp) of 0.525414 at a tip speed ratio of 8.75 and angle of attack of 6º was determined. From the values, the ideal chord distribution for the blade was determined as shown in Table 5.

Table 5. Chord Distribution

Radial Position (m)	Chord length (m)
0	0.108013
0.05	0.0755337

0.1	0.057693
0.15	0.0465504
0.2	0.0389749
0.25	0.0335026
0.3	0.0293694
0.35	0.0261396
0.4	0.0235473
0.45	0.0214212
0.5	0.0196463

By creating a wind field with the following parameters, mean wind speed 3.79 m/s, roughness length of 0.001m and turbulence intensity 10% (selected based on a semi urban setting), the turbine power flow for the primary rotor was modeled as shown in Figure 4.

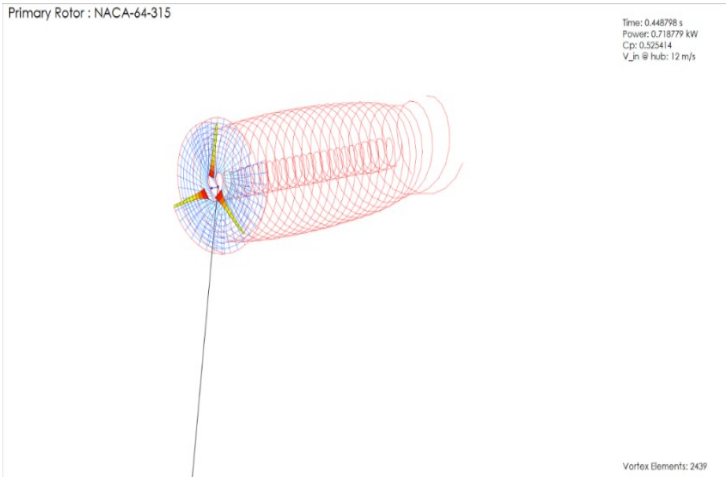

Figure 4: The simulated power flow of the primary rotor

From the model, the wake velocity as a function of the rotor separation (x) was determined as shown in equation (14):

$$v_{wake} = v_{\dot{\iota}} \left(\frac{2.44272}{0.36\,x^2 - 0.1656\,x + 4.938} \right) \quad \text{.....(14)}$$

By double differentiation a maximum wake velocity at a rotor distance of 0.23m was determined.

Hence, we obtain a maximum velocity of $v_{wake\_x=0.23} = 0.4356 v_{in}$

2.2.2. Secondary Rotor

From the wind field used for the primary rotor, the secondary rotor was modeled as a downwind turbine to allow for a counter rotation and as the same tip speed ratio (8.75) as the primary rotor (Figure 5).

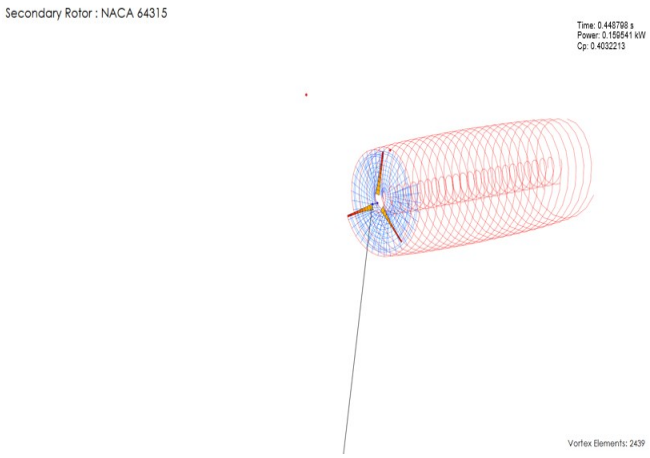

Figure 5:1 The simulated power flow of the secondary rotor

An individual power coefficient of 0.4032213 for the secondary rotor was determined. Therefore, the total power output was determined using equation (15):

$$C_p = \frac{Cp_{pri}\frac{1}{2}\rho A(v_1)^3 + Cp_{sec}\frac{1}{2}\rho A * \left[v_1\left(\frac{2.14272}{0.36x^2 - 0.1656x + 4.938}\right)\right]^3}{\frac{1}{2}\rho A {v_1}^3} \quad \ldots\ldots\ldots\ldots\ldots\ldots\ldots\ldots\ldots\ldots$$

(15)

Therefore, at a rotor separation of 0.23 m, the power coefficient for the system is 0.5599 or 55.99%

2.3. Determination of Power Coefficient

Sample power coefficient was calculated for rotor separation (x) = 2.75 m at the second fan speed of 4.747 m/s:

Primary Rotor speed = 396.125 rpm

Rotational Speed (ω) = (396.125*2*π)/60 = 41.482 rad/s

∴ Tip Speed Ratio$_{primary}$ = (r*ω)/v = (41.482*0.5)/4.747= 4.369

Axial Induction Factor = (fan speed – rotor speed)/fan speed = (4.747– 4.156)/4.747 = 0.1245

$C_{p\_primary} = 4a\,(1-a)^2 = 4*0.1245(1-0.1245)^2 = 0.3817$

Kinetic Energy per second absorbed by the rotor$_{primary}$ = $1/2*\rho*\pi*r^2*v^3*Cp_{pri}$ ……(16)

$= 0.5*1.225*\pi*0.5^2*4.787^3*0.3817$

= 20.1422 W

For the secondary rotor,

The secondary rotor rpm = 88.398

Rotational Speed (ω) = (88.398*2*π)/60 = 9.257 rad/s

∴ Tip Speed Ratio$_{secondary}$ = (r*ω)/v = (9.257*0.5)/1.886 = 2.454

Since there are two ultrasonic sensors, the wind velocity exiting the second rotor was measured, hence the power generated was determined through alternative means.

Using the Tangential Force Equation [15]

Where, F_T is the tangential force, U is the incoming wind speed, c is the average chord length, C_l and C_d are the lift and drag coefficients and α is the angle of attack.

$$F_T = \frac{1}{2}\rho U^2 c\left(C_l \sin|\alpha| - C_d \cos|\alpha|\right) \quad \text{……..……..(17)}$$

$F_T = 0.5*1.225*1.938^2*0.074*¿$

The torque acting by the rotor turning is $Q = BH\,F_T$.

Where, B is the number of Blades and H is the rotor height

Therefore, the torque of the secondary rotor is equal to 3*1*0.02383= 0.07149 Nm. Thus, we recall Power generated is given equal to Torque*Rotational Speed.

Therefore, Power$_{secondary}$ = 0.07149*9.527 = 0.6811 W

Hence, C_p = Power Generated by Torque/Power in the Wind……..(18)

$C_{psecondary}$ = 0.6811/ (0.5*1.225* π*0.5^2*1.938^3) = 0.6811/3.577 = 0.1904 = 19.04%

Therefore, Total Power generated by the system = 20.1422 + 0.6811 = 20.8233 W

C_p of the system = 20.8233/ (0.5*1.225* π*0.5^2*4.747^3) = 20.8233/51.458= 0.4047.

$\therefore$ C_p gain = $C_{p\_system} - C_{p\_primary}$ .....……..…..(19)

= 0.4047 – 0.3817 = 0.023 = 2.3% increase in power

3. Methodology

The pilot scale was designed as shown in Figure 6. It features the two rotors coaxially mounted on to two pillow block bearings. The bearings are secured on a piece of plywood using nuts and bolts. Two stools were used as a support for the plywood. The speed and air flow sensors were installed to determine the performance parameters.

Figure 6. The coaxially rotor setup

3.1. Arduino Electronic System

The Arduino electronic system was designed to record the inlet flow wind speeds as well the rotational speed of the rotors as shown in Figure 7. In addition to the RPM sensor, a velocity sensor was constructed using an ultrasonic sensor (located at the entry of the wind tunnel) that came with the kit. Unlike the RPM sensor the ultrasonic sensor required no further signal processing. The Arduino system is powered using the computer itself. The following is a list of the components that comprises the electronic system: Arduino Mega 2560 Controller (used to send coded programs to electronic components and receive signals from components and transmit to the computer), Two RPM Sensors (records the rpm of the rotor), Two Ultrasonic

sensors (used to determine the incoming velocity of the air), LM 324 OP amp (used to condition the signal of the RPM sensor), Breadboard (used to create power rails in between electronic components). The code was programmed in the open source Arduino IDE using C++ syntax.

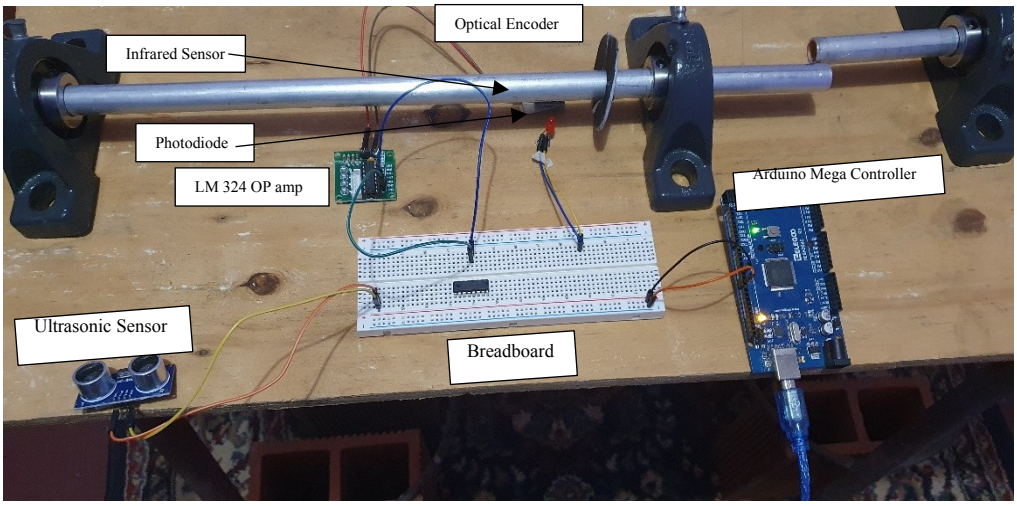

Figure 7. Experimental setup of the Arduino system

3.2. Air Study

An air study was conducted to optimize the turbine blades to a local climate of Trinidad and Tobago, it was determined that a NACA 64–315 air foil would be the most optimum for the conditions.

Using the Rainwise Portlog Weather Station, the equipment was set up on top of the roof of the University of the West Indies Mechanical Engineering laboratory (20 m high). The equipment was used to take readings in two-minute intervals for 2 days. One thousand four hundred and forty (1440) wind speed readings, wind direction, humidity ratio and other weather factors were recorded. The values for the wind speed were plotted against time as shown in Figure 8. From the figure an average wind speed of 3.79 m/s was seen. However, due to the large standard deviation that occurs, a more conservative estimate for the wind speed was chosen. Since 87.77% of the wind speeds recorded fall below 7 m/s, thus a rated speed of 7 m/s was used for the design. Using this value, a Reynold's Number of 478,650 and a Mach

Number of 0.021 was determined when the atmospheric properties calculator by the NACA was used.

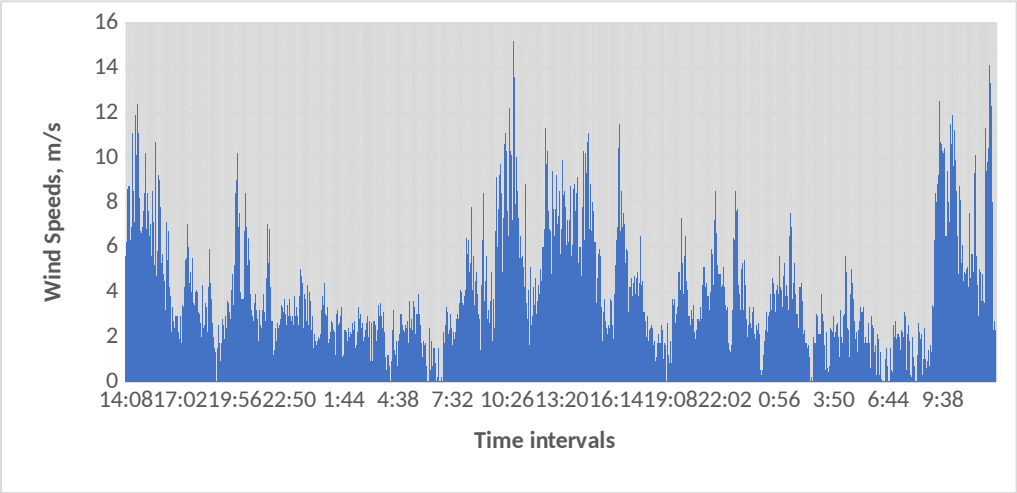

Figure 8:2 wind speeds recorded over the period of the study

3.3. Airfoil Selection

According to NACA, for low wind speeds, to reduce aerodynamic losses, an airfoil with a deep cambers and high aspect ratio should be chosen. Five of the most common airfoils with deep cambers and aspect ratio, were chosen for this study. These include, NACA 64–315, NACA 0012, Clark–Y, Falcon–II and the NACA 64–312. Using a Reynold's number and Mach number calculated from the study, these airfoils were inputted into XFOIL and values for the CL/CD for varying angles of attack were obtained and these data were plotted on the Airfoil Comparison. From Figure 10, it was discovered that the NACA 64–315 (Figure 9) has the highest CL/CD at an angle of attack of 6º, therefore NACA 64–315 was chosen as the airfoil used to design the blade for this study and its cross-section is shown in Figure 11.

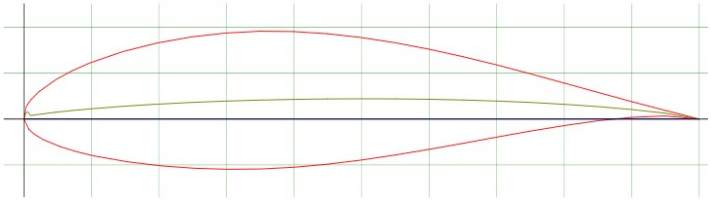

Figure 9. NACA 64-315

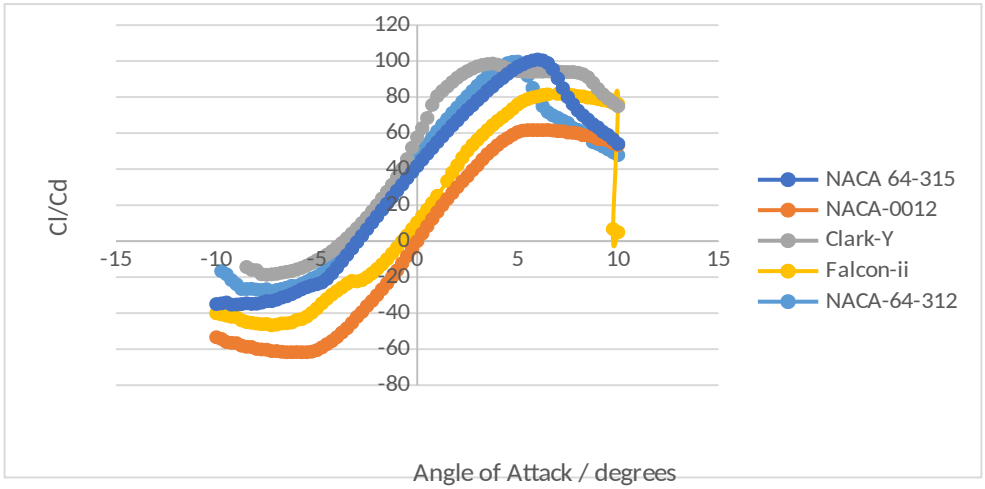

Figure 10. Comparison of airfoils at varying angles of attack

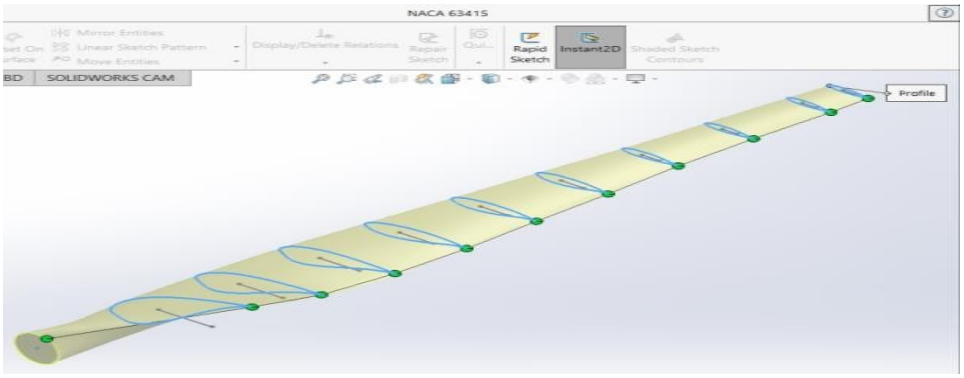

Figure 11. The NACA 64–315 cross-section of the blade

3.4. Material Selection

From the air study, an average relative humidity of 77% was observed over the tested period, meaning that the materials chosen from the turbine should have some corrosion-resistant properties. As the blades would experience bending forces due to the winds, a material with high yield strength was chosen. The material should also have low density, so it possesses little inertia to overcome. Aluminum possesses these qualities and is cheap compared to other alloys. However, the blades would be under great cyclic stress (as the machine would be working all the time), hence a material with high fatigue stress should be chosen. From the fatigue strength chart, it is seen that a fiberglass epoxy would be the ideal choice for high fatigue strength, in addition to the material being cheap. The fiberglass blades were reinforced

with cedar wood, which is low cost, light weight and high strength. The Nacelle of the turbine was made from a corrosion-resistant plastic composite. The shafts of turbines was made from 6061−aluminum as it has high yield strength and fatigue strength with the added benefit of low cost and availability compared to other stainless steels. The tower was made from standard 11-gauge galvanized steel, like those on electrical poles, as it would be easy to procure. The foundation was made from reinforced concrete to prevent rocking moments and ensure a stable base for the turbine. The internal components were sourced from standardized parts.

3.5. Design Process

To strike a balance between safety and cost, design calculations are done to determine the minimum dimensions of materials used to fabricate the prototype.

3.6. Testing and Data Collection

After the pilot scale was completed, it was tested at different wind speeds and at different rotor separation distances, for a fixed tip speed ratio.

An experiment was conducted to verify the theoretical and simulated data that were presented earlier in the report.

3.6.1 Required Apparatus

(i) Wind Tunnel as assembled

(ii) 20-inch, 3-speed LASKO Fan

(iii) Arduino Electronic System with RPM and velocity sensor

(iv) Computer to connect the Arduino to and collect data

3.6.2 Experimental Procedure

(i) Set-up apparatus as demonstrated with the rotors

(ii) Place LASKO fan 0.3 meters away from the ultrasonic sensor

(iii) Start the fan on speed 1 and wait until a constant velocity reading is seen and record this velocity

(iv) Repeat this step for the other two speeds

(v) Install the rotors 3 meters apart on the shaft locking them in place using the grub screw. Bolt the bearing onto the plywood to lock them into place.

(vi) Turn on the fan at speed 1 and wait until a constant rpm is recorded for both rotors and then record the rpm

(vii) Repeat step vi for the other two speeds of the fan

(viii) Repeat steps (v) to (vii) for different rotor separation distances ranging from 2.75 to 0.25m and record results.

3.6.3 Recorded Wind Velocity

The experimental wind velocities were gathered using the airflow ultrasonic sensor and the rpm values were recorded using the rpm data collected by the Arduino. Table 6 shows the data recorded from the Arduino. Table 7 shows the experimental results of dynamic rotor test.

Table 6. Lasko Fan Wind Speed

Speed Rating No.	Recorded Wind Velocity
1	3.488
2	4.747
3	6.258

Table 7. Experimental Results of Dynamic Rotor Test

Rotor Separation (x), m	Wind Velocity after passing through the primary rotor (v), m/s			Wind Velocity incoming to the secondary rotor (v),			Primary Rotor RPM			Secondary Rotor RPM		
	1st Speed	2nd Speed	3rd Speed	1st Speed	2nd Speed	3rd Speed	1st Speed	2nd Speed	3rd Speed	1st Speed	2nd Speed	3rd Speed
3.00	3.169	4.155	5.459	1.393	1.886	2.769	284.76	396.32	547.85	63.92	85.845	115.30
2.75	3.172	4.156	5.457	1.434	1.938	2.822	284.64	396.12	547.85	65.60	88.398	118.82
2.50	3.169	4.156	5.457	1.477	1.992	2.884	284.84	396.00	548.32	67.32	91.028	122.45
2.25	3.169	4.155	5.456	1.520	2.047	2.945	284.74	396.12	548.03	69.09	93.736	126.19
2.00	3.170	4.155	5.457	1.565	2.103	3.004	284.54	396.08	547.93	70.90	96.524	130.05
1.75	3.169	4.155	5.458	1.611	2.161	3.066	284.22	396.58	547.84	72.76	99.395	134.02
1.50	3.170	4.154	5.457	1.659	2.220	3.129	284.32	397.00	547.66	74.67	102.35	138.11
1.25	3.169	4.155	5.457	1.708	2.281	3.193	285.00	396.43	547.33	76.63	105.39	142.33
1.00	3.169	4.154	5.457	1.758	2.344	3.259	284.84	396.63	547.47	78.64	108.53	146.67
0.75	3.172	4.155	5.454	1.810	2.409	3.326	284.75	396.54	547.05	80.70	111.76	151.15

0.50	3.168	4.155	5.457	1.863	2.475	3.395	284.54	395.85	547.24	82.82	115.08	155.77
0.25	3.169	4.157	5.457	1.926	2.543	3.464	284.81	396.34	547.54	84.99	118.50	160.53

4. Results and Discussions

4.1. Comparison of the Tip Speed Ratio with Fan Speed for the Primary Rotor

Figure 12 illustrates the comparison of the tip speed ratio with the fan speed for the primary rotor. Note that the standard deviation between the different rotor separation tests is quite minuscule, hence an average of the values can be determined. From Figure 12 it was discovered that as the fan speed increases the tip speed ratio increases thus demonstrating a positive linear relationship between the two variables.

4.2. Comparison of the Tip Speed Ratio with Fan Speed for the Secondary Rotor

Figure 13 illustrates the comparison of the tip speed ratio with the fan speed for the secondary rotor with rotor separations between 0.25 m and 3 m at intervals of 0.25 m. Each series shows a positive linear relationship between tip speed ratio and fan speed. The smallest rotor separation (x=0.25 m) shows the largest tip speed ratio, while the largest rotor separation distance (x=3 m) has the smallest tip speed ratio at a fan speed of 1m/s.

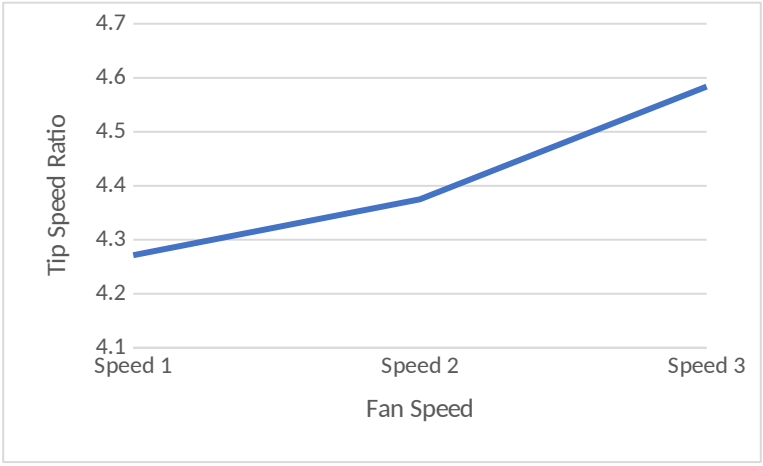

Figure 12. Comparison of the Tip Speed Ratio with Fan Speed (Primary Rotor)

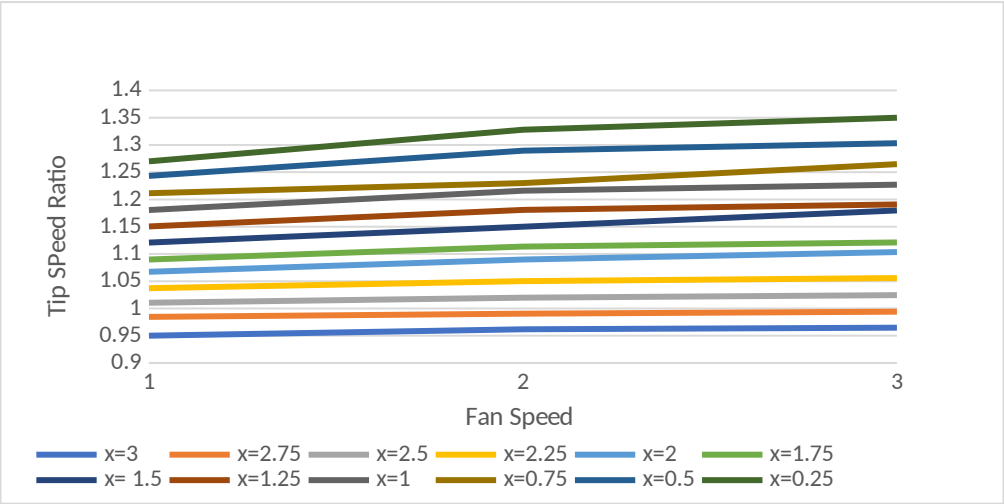

Figure 13. Comparison of the Tip Speed Ratio with Fan Speed (Secondary Rotor)

4.3. Comparison of the Tip Speed Ratio with Rotor Separation for the Secondary Rotor

Figure 14 shows the comparison of the tip speed ratio with the rotor separation for the secondary rotor. The graph demonstrates an inverse relationship between the tip speed ratio and rotor separation. It was discovered that the three series start (at x=3 m) but diverge away from each other. It is an indication that as the speed increases the tip speed ratio also increases exponentially.

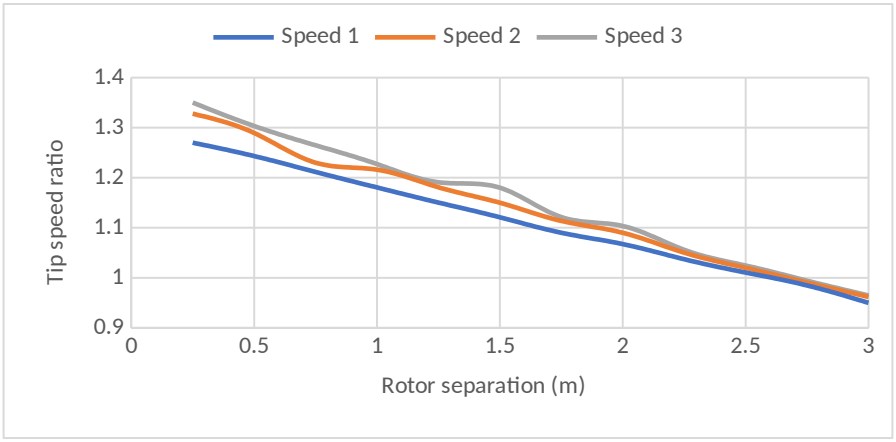

Figure 14. Comparison of the Tip Speed Ratio with Rotor Separation (Secondary Rotor)

4.4. Comparison of the total power with rotor separation

A comparison of the total power with a rotor separation is shown in Figure 15. It shows the power gained by the three speeds, with power at the three speed being the highest. However, there is a small positive gradient seen in each line, indicating that as the distance between the

rotors decreases the power increases. The gradient of each series increases with increasing speed.

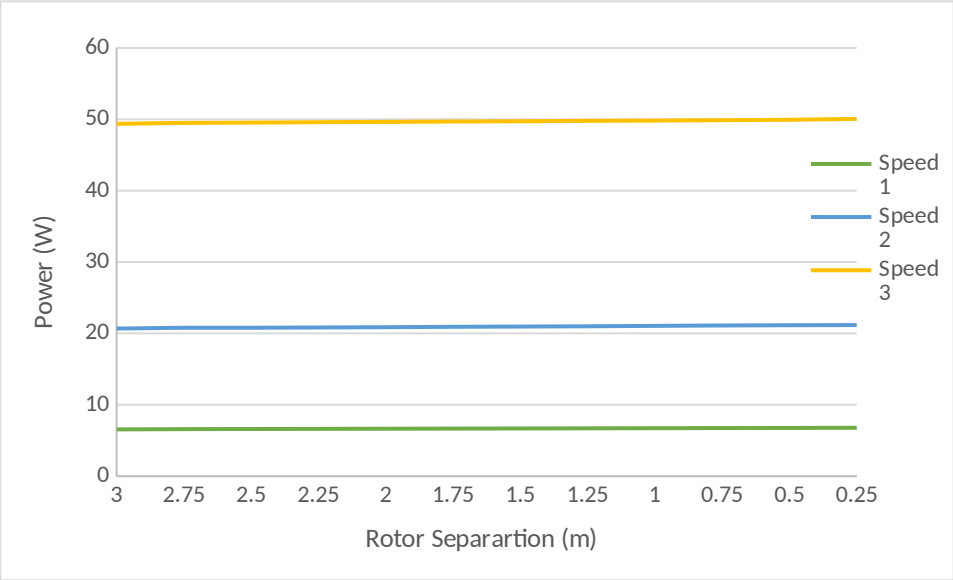

Figure 15. Comparison of the total power with rotor separation

4.5. Comparison of the power coefficient gain with rotor separation

Figure 16 illustrates the gain in power coefficient in response to variations to the distance between the rotors. It shows a negative linear relationship between the rotor separation and power coefficient gain. The higher speed corresponds to a greater gain in the power coefficient.

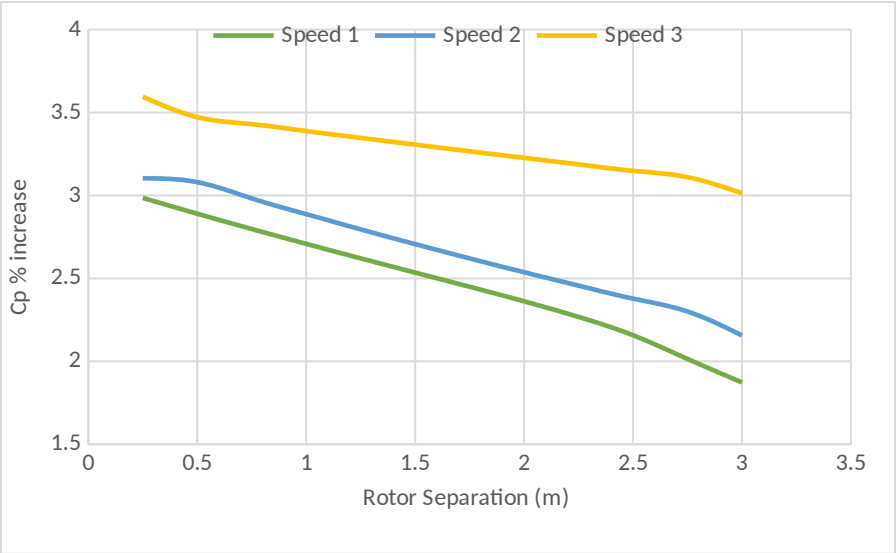

Figure 16. Comparison of the power coefficient gain with rotor separation

4.6. Comparison between the experimental and simulation results for power coefficient and rotor separation

Figure 17 shows the various power coefficients of the dual rotor system in relation to the rotor separation. The graph shows the comparison between the experimental and QBlade simulation results for power coefficient and rotor separation. The power coefficient derived from the simulation is higher than that from experimentation. The R^2 values, which is an indication of strength between dependent and independent variables show similar values for each model, indicating a strong statistical relationship between simulation and experimental methods of evaluating the power coefficient.

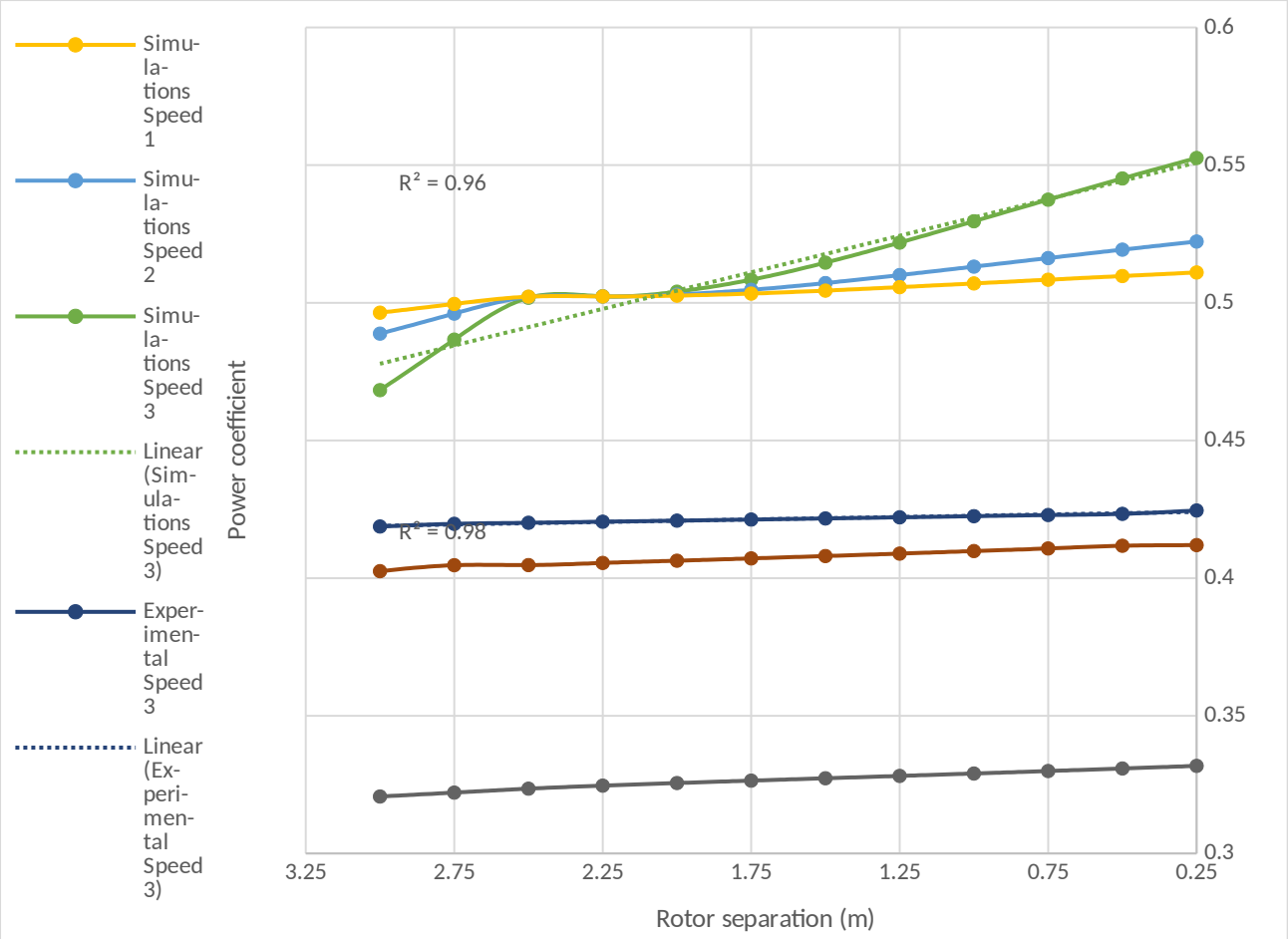

Figure 17. Comparison between the experimental and simulation results for power coefficient and rotor separation

The stationary air particles collide with the fast-moving air particles as they move through the stagnant air past the rotor. The collision causes the air mass to continue moving in the same direction it was before. Because of losing momentum due to impulse-momentum consistency, the air particles slow down. Since momentum is directly proportional to velocity, the longer the particles travel, the more momentum they lose, decreasing the wind speed over the distance traveled. Furthermore, these particles collide in three dimensions with stationary particles, causing the fast-moving particles to deviate from their intended path. This effect is responsible for the turbulent wake velocity observed in the simulation, as well as the decrease in wind velocity after passing through the wind turbine rotor. Furthermore, these particles spread out, covering a much wider region than air particles do. As the volume of flow increases, the velocity decreases, according to the flow continuity equation. Since the tip speed ratio is a function of incoming wind velocity, explains why the tip speed ratio decreases

dramatically from the primary to the secondary rotor. Even though the same wind stream that passes through the primary rotor also passes through the second rotor, the wind velocity is slightly lower. Regardless, there is kinetic energy in the air that can be used. Note that higher speeds entering the primary side of the system result in higher wind velocities leaving and, as a result, higher secondary rotor tip speed ratios. The secondary wind turbine will work as planned with higher tip speed ratios, resulting in higher power coefficients.

With respect to the relationship between power coefficient and rotor separation, it is observed that as the two rotors came closer together, the power coefficient increased as well. This phenomenon is valid for the QBlade simulations and the experimental results. According to the principle discussed earlier, the velocity decreases as the distance between the two points decreases. Since power is directly proportional to velocity, power should decrease as distance increases, as the results indicate.

The simulated induced wake velocity was higher than anticipated, indicating that the primary rotor's power coefficient should be lower in the simulation. The experimental results were lower when compared to the simulation-predicted outcomes. The reduction is due to the errors in the manufacturing process. In addition, the blade was designed for a rated speed of 7 m/s that the Lasko fan never produce. Additionally, the mechanical components were sized for maximum of 16 m/s with an additional factor of safety inbuilt as well. This situation could result to unnecessary rotor inertia in the system which may have caused the rotors to not achieve their desired tip speed ratio.

The Newman multi-actuator disk theory predicted that a dual rotor wind turbine's overall power coefficient would increase, and the results of this experiment back up the theory [7]. However, unless the economic benefits outweigh the added expense of producing and building the secondary turbine, this power coefficient gain would not be feasible.

5. Conclusion

The rotating blade of a single-rotor propeller generates a lot of tangential or rotational air flow, which is wasted energy that could be used if a second rotor positioned behind the first takes advantage of the disturbed airflow and extracts up to 40% more energy from a given swept area than a single rotor.

This study conducted the simulation and experimental analysis on a designed dual rotor horizontal axis wind turbine (DRHAWT).

The study examines the analysis of air flow and the optimization of the air foil design, using computational fluid dynamics, to maximize lift force. A proper wind study was conducted, including the development of a proper psychometric study of the air from which the Reynold's number was obtained. After the wind study was conducted, the airfoil of the turbine most ideal for the conditions was selected and the wind turbine was design and then modified to a pilot scale model in the form of a testing rig. The testing was built to validate the theory researched and the following was achieved:

(i) The testing rig operated slightly below the simulations.

(ii) Larger Incoming Velocity allowed the rotors to achieve higher tip speed ratios.

(iii) The smaller the rotor separation distance, the larger the power gain.

(iv) At an incoming wind velocity of 6.258 m/s a tip speed ratio of 4.584 and 1.35 were observed for the primary and secondary rotors, respectively, at a rotor separation distance of 0.25 meters. These results produced a system power coefficient of 42.46% accounting for a power gain of 3.6% extra compared to a single rotor wind turbine.

Further Investigation into the wake velocities should be undertaken, using RANS simulation. From the Jensen wake model [12], it was seen that the area of overlap ratio contributed to the strength of the wake velocity. Therefore, further investigation should be conducted by varying

the size of the secondary rotor, using a dedicated secondary blade that will maximize the kinetic energy of the wind downwind, so the overall system's efficiency would increase.

References

[1] IRENA. Renewable Energy Statistics (2020). International Renewable Energy Agency: Abu Dhabi, United Arab Emirates, 2020.

[2] GWEC. Global Wind Report 2019; Global Wind Energy Council: Brussels, Belgium, 2020.

[3] Offshore Wind Turbine SG 14-222 DD I Siemens Gamesa.

Available online: https://www.siemensgamesa.com/en-int/productsand-services/offshore/wind-turbine-sg-14-222-dd (accessed on 13 July 2020).

[4] Kumar P. S, Abraham A, Bensingh R. J. and Ilangovan S. (2013). "Journal of Scientific & Industrial Research 72".

[5] Jung, S.N., No, T.-S., Ryu, K.-W., Aerodynamic performance prediction of a 30 kW counter-rotating wind turbine system, in Renewable Energy 30, pg. 631– 644, 2005.

[6] Oprina G., Chihaia R.A., El-Leathey L.A., Nicolaie S., Băbuțanu C.A., Voina A.(2016) A Review On Counter-Rotating Wind Turbines Development. Journal of Sustainable Energy Vol.7, No.3, September, 2 ISSN2067-5534,2016.

[7] Newman, B.G. (1986) Multiple Actuator-Disc Theory for Wind Turbines, in Journal of Wind Engineering and Industrial Aerodynamics, vol. 34, pg. 215-225, issue 3.

[8] Chantharasenawong, C., Suwantragul, B., Ruangwiset, A. (2008) Axial Momentum Theory for Turbines with Co-Axial Counter Rotating Rotors, Commemorative International Conference of the Occasion of the 4th Cycle Anniversary of KMUTT Sustainable Development to Save the Earth: Technologies and Strategies Vision 2050: (SDSE2008) Bangkok, Thailand. 11-13 December 2008.

[9] Appa, K. (2002) Energy Innovations Small Grant (EISG) Program (Counter Rotating Wind Turbine System), EISG Final Report, (California, US).

[10] Rosenberg, A; Selvaraj, S; and Sharma, A. (2014). A Novel Dual-Rotor Turbine for Increased Wind Energy Capture. Journal of Physics: Conference Series, Volume 524, The Science of Making Torque from Wind 2014 (TORQUE 2014) 18–20 June 2014, Copenhagen, Denmark.

[11] Milind Deotale, Abhishek Chavan, Abhishek Patil, (2018) Co-Axial Rotor Wind, Turbine Bhavesh Patil 1, IJARSE ISSN 23198354, vol 7 dated 7 April 2018.

[12] Peña, Alfredo, Pierre-Elouan Réthoré, and M. Paul van der Laan. (2015) "On The Application of the Jensen Wake Model Using a Turbulence-Dependent Wake Decay Coefficient: The Sexbierum Case". Wind Energy 19 (4): 763-776. doi:10.1002/we.1863.

[13] Wilson, R. E., P. B. S. Lissaman, M. James, and W. R. McKie. (1983) "Aerodynamic Loads on a Darrieus Rotor Blade". Journal of Fluids Engineering 105 (1): 53-58. doi:10.1115/1.3240940.

[14] Trinidad and Tobago Metrological Service. https://www.metoffice.gov.tt/.

[15] Manwell, J. F., McGowan, J. G. and Anthony L. Rogers. (2011). Wind Energy Explained: Theory, Design and Application. Chichester, U.K.: John Wiley & Sons, Ltd.

Authors' information

University of West Indies, Mechanical and Manufacturing Engineering Department, St. Augustine, Trinidad and Tobago.
Corresponding Author Email: anthony.adeyanju@sta.uwi.edu

Dr. Adeyanju Anthony obtained his Ph.D. in Mechanical Engineering at the University of the West Indies, St. Augustine Campus in 2012, his M.Eng. in Mechanical Engineering at the University of Ado Ekiti, Nigeria in 2007, his B.Eng. in Mechanical Engineering at Ondo State University, Nigeria in 1994 and his Postgraduate Certificate in University Teaching and Learning (CUTL) in 2018.

He received the UWI-NGC 2014 Research Awards as the Most Outstanding Graduate Researcher 2011/2012.

He has industrial experience at the Nigerian National Petroleum Corporation (NNPC), Concord Airline and Gas Airline in Nigeria. He is a registered engineer with the Council of Regulation of Engineering in Nigeria (COREN) and a member of Nigerian Society of Engineers (NSE). He is an academic member of ATINER, Greece and a senior member of CBEES,.Hong Kong.

His research interests include solar/thermal energy, hydropower, geothermal, biomass/biogas, heat transfer, refrigeration, air-conditioning, gas and steam turbine.